GEOPHYSICS, VOL. 82, NO. 6 (NOVEMBER-DECEMBER 2017); P. O83–O89, 6 FIGS.
10.1190/GEO2017-0196.1

Multiazimuth coherence

Jie Qi[1], Fangyu Li[1], and Kurt Marfurt[1]

ABSTRACT

Since its introduction two decades ago, coherence has been widely used to map structural and stratigraphic discontinuities such as faults, cracks, karst collapse features, channels, stratigraphic edges, and unconformities. With the intent to map azimuthal variations of horizontal stress as well as to improve the signal-to-noise ratio of unconventional resource plays, wide-/full-azimuth seismic data acquisition has become common. Migrating seismic traces into different azimuthal bins costs no more than migrating them into one bin. If the velocity anisotropy is not taken into account by the migration algorithm, subtle discontinuities and some major faults may exhibit lateral shifts, resulting in a smeared image after stacking. Based on these two issues, we evaluate a new way to compute the coherence for azimuthally limited data volumes. Like multispectral coherence, we modify the covariance matrix to be the sum of the covariance matrices, each of which belongs to an azimuthally limited volume, and then we use the summed covariance matrix to compute the coherent energy. We validate the effectiveness of our multiazimuth coherence by applying it to two seismic surveys acquired over the Fort Worth Basin, Texas. Not surprisingly, multiazimuth coherence exhibits less incoherent noise than coherence computed from azimuthally limited amplitude volumes. If the data have been migrated using an azimuthally variable velocity, multiazimuth coherence exhibits higher lateral resolution than that computed from the stacked data. In contrast, if the data have not been migrated using an appropriate azimuthally variable velocity model, the misalignment of each image results in a blurring of the multiazimuth coherence and the coherence computed from the stacked data. This suggests that our method may serve as a future tool for azimuthal velocity analysis.

INTRODUCTION

Seismic attributes are routinely used to quantify changes in amplitude, dip, and reflector continuity in seismic amplitude volumes. Coherence is an edge-detection attribute that maps lateral changes in waveforms, which may be due to structural discontinuities, stratigraphic discontinuities, pinchouts, or steeply dipping coherent noise cutting more gently dipping reflectors. Several generations of coherence algorithms have been introduced and applied to geologic discontinuity detection, such as crosscorrelation (Bahorich and Farmer, 1995), semblance (Marfurt et al., 1998), the eigenstructure method (Gersztenkorn and Marfurt, 1999), the gradient structure tensor (Bakker, 2002), and predictive error filtering (Bednar, 1998) algorithms. All those algorithms operate on a spatial window of neighboring traces (Chopra and Marfurt, 2007).

Bahorich and Farmer's (1995) crosscorrelation algorithm searches along candidate dips for the highest positive normalized crosscorrelation coefficient between the pilot trace and the nearest two or four neighboring traces in the inline and crossline directions resulting in values between 0 (incoherent) and 1 (coherent). Marfurt et al.'s (1998) semblance algorithm computes the ratio of the energy of the average trace to the average energy of all the traces in an analysis window. To improve the semblance for fault detection, some authors (Hale, 2013; Wu and Hale, 2016; Wu et al., 2016) apply fault-oriented smoothing to the numerator and denominator of the semblance ratio to compute a fault-likelihood value. Gersztenkorn and Marfurt's (1999) eigenstructure-based coherence algorithm first computes a covariance matrix from a window of trace segments oriented along a structural dip. In this algorithm, coherence is computed as the ratio of the first eigenvalue to the sum of all the eigenvalues of the covariance matrix. The energy-ratio coherence algorithm (Chopra and Marfurt, 2007) also uses a covariance matrix, from windowed analytic traces (the original data and its Hilbert transform), and estimates the coherent component of the data

Manuscript received by the Editor 30 March 2017; revised manuscript received 19 May 2017; published ahead of production 13 July 2017; published online 29 August 2017.
[1]University of Oklahoma, ConocoPhillips School of Geology and Geophysics, Norman, Oklahoma, USA. E-mail: jie.qi@ou.edu; fangyu.li@ou.edu; kmarfurt@ou.edu.

using a Karhunen-Loève (KL) filter. Like semblance, energy-ratio coherence is the ratio of the energy of the coherent (KL filtered) analytic traces to that of the original analytic traces. Bakker (2002) computes a version of coherence called "chaos" by computing eigenvalues of the gradient structure tensor. The 3×3 gradient structure tensor is computed by crosscorrelating derivatives of the seismic amplitude in the x-, y-, and z-directions. The first eigenvalue represents the energy of the data variability (or gradient) perpendicular to the reflector dip. If the data can be represented by a constant-amplitude planar event, the chaos is equal to -1.0. In contrast, if the data are totally random, the chaos is equal to $+1.0$. Similarly, Wu (2017) computes directional structure-tensor-based coherence for detecting seismic faults and channels. Closely related to coherence is Luo et al.'s. (1996) generalized Hilbert transform edge-detection algorithm, a long-wavelength version of Luo et al.'s (2003) Sobel filter discontinuity algorithm. Kington (2015) compares different coherence algorithms and exhibits the trade-offs among different implementations.

Picking discontinuities on vertical slices through the seismic amplitude volume is still the most common means to map faults on seismic data. However, coherence not only accelerates this process but also delineates channel edges, carbonate build-ups, slumps,

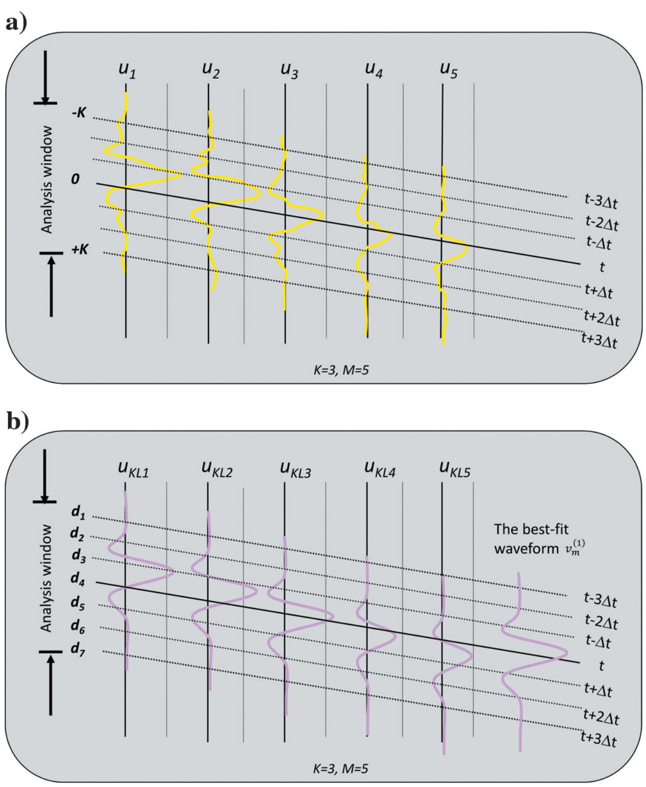

Figure 1. Cartoon of an analysis window with five traces and seven samples. (a) Five input traces ($\mathbf{U}_1 - \mathbf{U}_5$) extracted from a poststack seismic amplitude volume through the structural dip and (b) computed coherent traces ($\mathbf{U}_{\mathrm{KL}1} - \mathbf{U}_{\mathrm{KL}5}$) from five input traces. We use the semblance technique to compute inline and crossline structural dip components of each analysis point from the poststack image. Then, we build the analysis window by extracting its neighboring samples along the inline and crossline dips. The computations of coherent traces are introduced in Appendix A. Note that the wavelet amplitude of the three leftmost traces is about two times larger than that of the two rightmost traces.

collapse features, and angular unconformities (Sullivan et al., 2006; Schuelke, 2011; Qi et al., 2014). Coherence can also be used as an input seismic texture in multiattribute seismic facies analysis (Qi et al., 2016).

With the focus on shale resource plays, wide-azimuth surveys are commonly acquired to orient horizontal wells perpendicular to the maximum horizontal stress direction for optimum completion. Wide-azimuth surveys provide greater leverage against coherent noise such as ground roll and interbed multiples. Wide-azimuth, higher fold surveys also are amenable to modern surface-consistent statics solutions. The axes of azimuthal anisotropy are commonly aligned parallel and perpendicular with open fractures or microcracks. Finally, wide-azimuth surveys provide the data necessary for azimuthal anisotropy analysis. Several authors have computed attributes from azimuthally limited volumes with only moderate results. Barnes (2000) proposes a smoothing technique to reduce noise and spikes from instantaneous attributes computed from poststack data. Perez et al. (1999) compute spectral components from different azimuths and find it to be an indicator of anisotropy. Chopra and Marfurt (2007) find coherence computed from such lower-fold data to exhibit higher lateral resolution but also to be noisy. Al-Dossary et al. (2004) attempt perhaps the first interazimuth coherence algorithm but find it provides greater sensitivity to data quality than to geology.

A related problem is the computation of coherence from spectrally limited data volumes. Li and Lu (2014) and Li et al. (2015) compute coherence from different spectral components and corender them using a red, green, and blue (RGB) color model. Sui et al. (2015) add covariance matrices computed from a suite of spectral magnitude components, obtaining a coherence image superior to that of the original broadband data. Marfurt (2017) expands on this idea, adds coherence matrices computed from analytic spectral components (the spectral voices and their Hilbert transforms) along the structural dip, and obtains improved suppression of random noise and enhancement of small faults and karst collapse features.

In this paper, we build on this last piece of work, but we now generalize it to summing covariance matrices computed from a suite of azimuthally limited, rather than frequency-limited, volumes. We begin our paper with a review of the energy-ratio coherence algorithm. We then show the improved lateral resolution but reduced signal-to-noise ratio (S/N) of coherence images generated from azimuthally limited seismic data. Next, we show how the multiazimuth coherence computation provides superior results when applied to a data volume that has been properly migrated using an azimuthally varying velocity model. Finally, we apply the multiazimuth coherence algorithm to a data volume that has not been properly corrected for azimuthal anisotropy. We conclude with a summary of our observations and a short list of recommendations.

METHOD

Coherence is an edge-detection attribute that measures lateral changes in the seismic waveform and amplitude. The multiazimuth coherence algorithm is based on an energy-ratio coherence algorithm, which computes the ratio of coherent energy of seismic trace and total energy of seismic trace (Appendix A). Figure 1 shows $2K + 1 = 7$ sample vectors of length $M = 5$, where one sample vector is constructed from interpolation of samples from each of five traces. We use the semblance technique to compute inline and crossline structural dip components of one analysis point from the poststack image. Then,

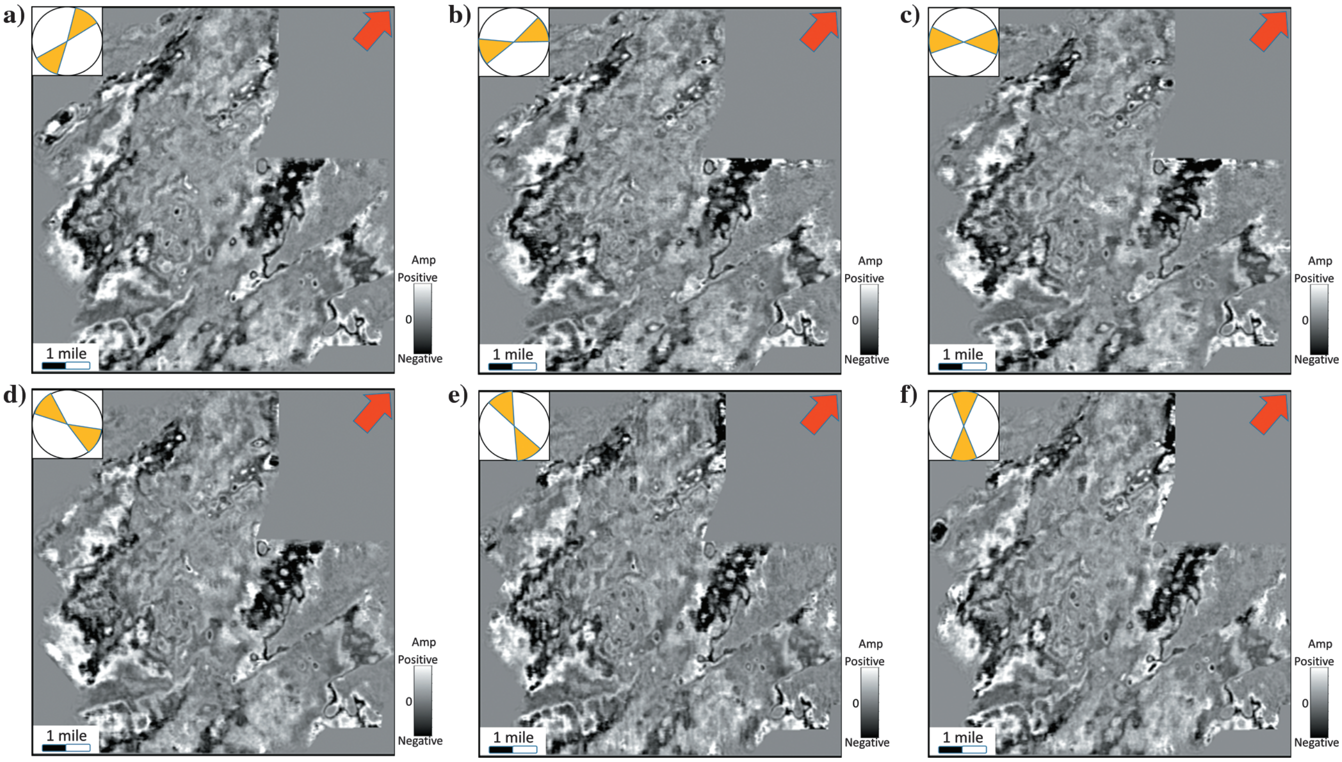

Figure 2. Time slices at $t = 0.74$ s through azimuthally limited migrated seismic amplitude (Amp) volumes: (a) 165°–15°, (b) 15°–45°, (c) 45°–75°, (d) 75°–105°, (e) 105°–135°, and (f) 135°–165°. Note the azimuthal variations and that although the S/N of each azimuthal sector is low, one can identify the faults and karst features.

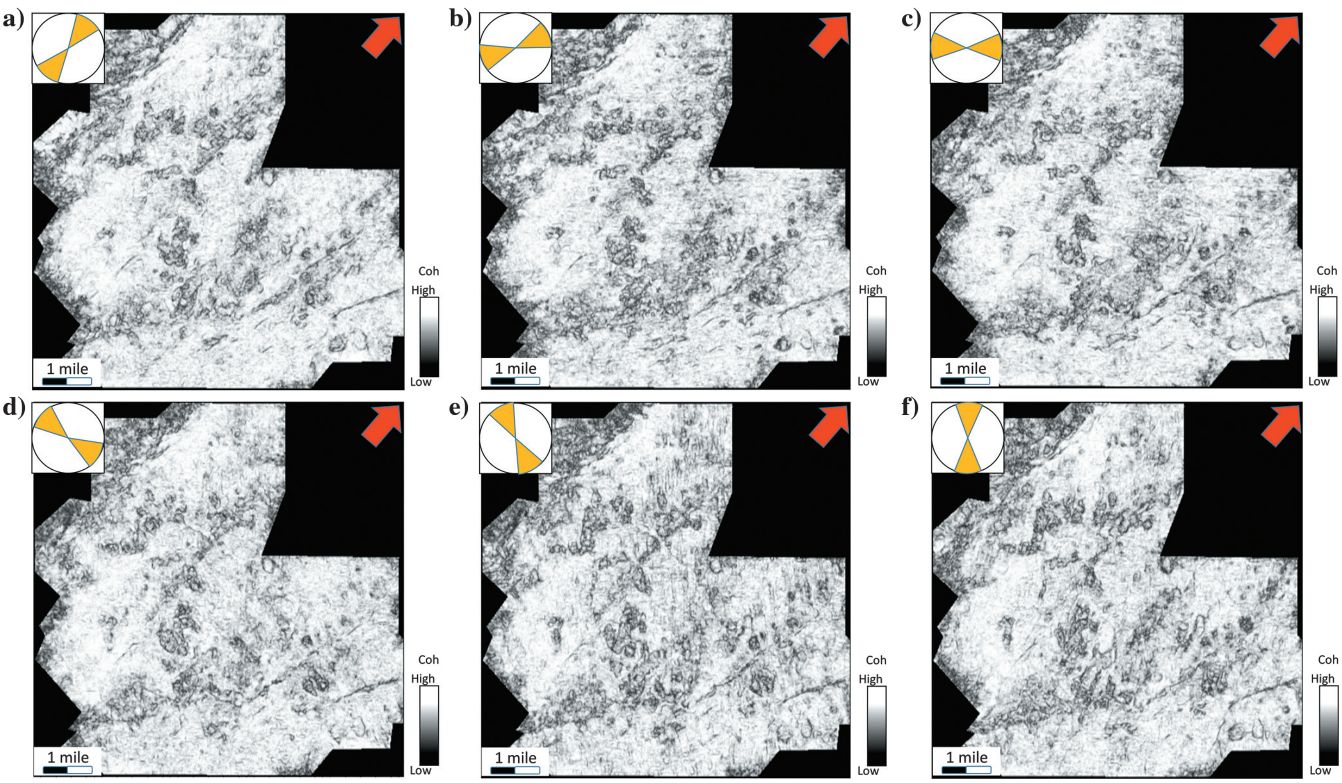

Figure 3. Time slices at $t = 0.74$ s through coherence (Coh) volumes computed from the azimuthally limited data shown in Figure 2: (a) 165°–15°, (b) 15°–45°, (c) 45°–75°, (d) 75°–105°, (e) 105°–135°, and (f) 135°–165°. Although one can identify faults and karst collapse features, the images are quite noisy.

we build the analysis window by extracting its neighboring samples through inline and crossline dips. The principal component (Karhunen-Loève) filtered traces are shown in Figure 1b. More details of the energy-ratio coherence algorithm are shown in Appendix A.

Migrating seismic traces into bins depending on the source-receiver orientation provides azimuthally limited seismic amplitude volumes. Using a migration isotropic velocity may give rise to imaging misalignments in high azimuthally anisotropic reservoirs. Stacking those seismic gathers along offset domains results in azimuthally limited seismic amplitude volumes. Coherence computed from the poststack volume that stacking all azimuthally limited seismic amplitude volumes exhibits fewer geologic details and lower lateral resolution of migrated seismic images than coherence computed from azimuthally limited seismic amplitude volumes (Chopra and Marfurt, 2007). Stacking these azimuthally limited amplitude volumes can suppress random noise. We will show that coherence computed from the full stack is generally less noisy than that computed from azimuthally limited volumes.

Multiazimuth coherence

We generalize the concept of energy-ratio coherence by summing J covariance matrices $\mathbf{C}(\varphi_j)$ computed from each of the J azimuthally sectored data volumes:

$$\mathbf{C}_{\text{multi}-\varphi} = \sum_{j=1}^{J} \mathbf{C}(\varphi_j). \tag{1}$$

The summed covariance matrix is of the same $M \times M$ size as the original single-azimuth covariance matrix, but it is now composed of J times as many sample vectors. As the conventional covariance matrix, the multiazimuth covariance matrix is a symmetric positive definite matrix. Eigendecomposition of the multiazimuth covariance matrix is a nonlinear process, such that the first eigenvector of the summed covariance matrix is not a linear combination of the first eigenvectors computed for the azimuthally limited covariance matrices, in which case the resulting coherence would be the average of the azimuthally limited coherence computations.

Geologic details in each azimuthally seismic image are transferred into sample vectors. Summing the sample vectors provides a means of summing geologic anomalies into the multiazimuth covariance matrix, such as stacking up azimuthally limited coherence. This nonlinear eigendecomposition of the multiazimuth covariance matrix has advantages in suppressing random noise that would help deal with random noise in azimuthally limited seismic volumes. To lessen the computation cost, azimuths are commonly binned into six 30° or eight 22.5° sectors, although finer binning is common in large processing shops.

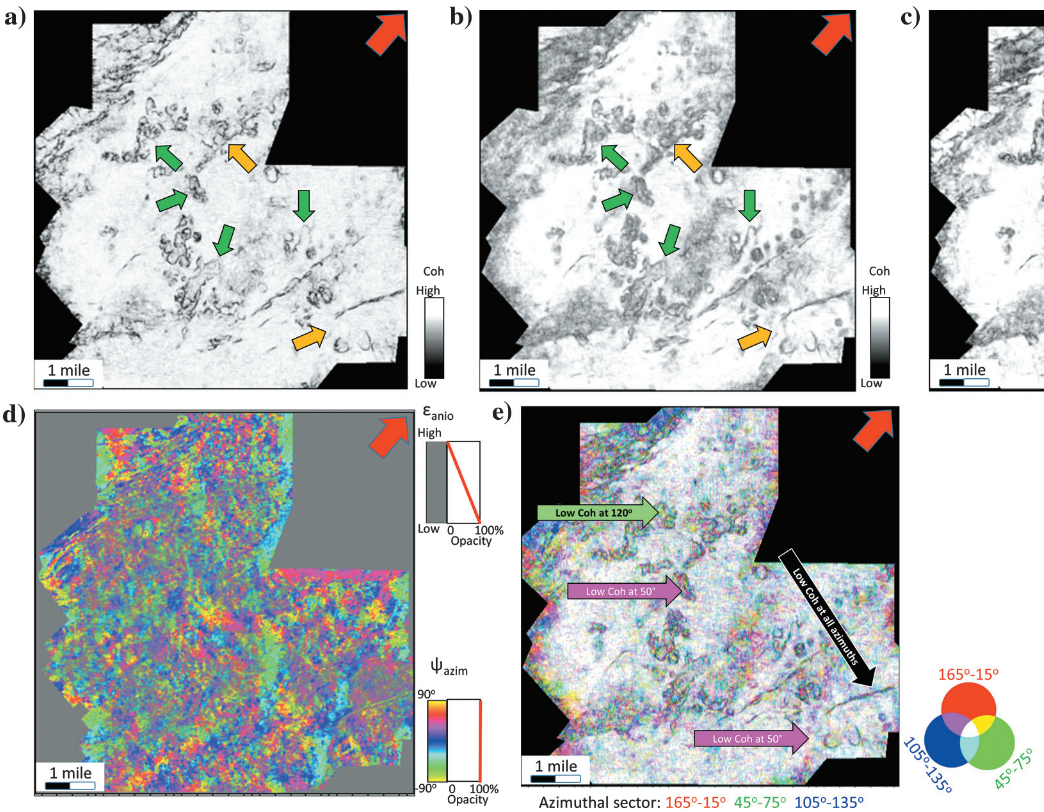

Figure 4. Time slices at $t = 0.74$ s through the coherence volume computed from (a) the poststack seismic amplitude data, (b) the sum of the coherence shown in Figure 3, (c) the multiazimuth coherence, (d) the top Marble Fall limestone through the corendered anisotropic intensity $\varepsilon_{\text{anis}}$ and azimuth ψ_{azim}, and (e) the RGB image computed by azimuthal sectors 165°–15°, 45°–75°, and 105°–135°. Note that there is improved lateral resolution of the multiazimuth coherence. Edges of karst features (indicated by green arrows) are better delineated, and subtle discontinuities (indicated by yellow arrows) are as strong as major faults. The result obtained by stacking the azimuthal coherence volumes is as noisy as places in other slices. The corendered anisotropic intensity $\varepsilon_{\text{anis}}$ and azimuth ψ_{azim} images indicate areas with high anisotropic effects, which also correspond to lateral variation areas, where there are colorful areas in the RGB corendered image.

Application

Our two examples are from the Fort Worth Basin, Texas. Survey A was acquired in 2006 using 16 live receiver lines forming a wide-azimuth survey with a nominal 16.7×16.7 m (55×55 ft) common-depth point (CDP) bin size. The data were preprocessed and binned into six azimuths, preserving the amplitude fidelity at each step before prestack time migration (Roende et al., 2008). A 3 trace × 3 trace × 7 sample (inline axis × crossline axis × vertical axis) analysis window is used to compute coherence. In general, smaller windows are better if the S/N allows it. Vertical windows larger than the dominant period smear stratigraphic edges. Figure 2 shows time slices at $t = 0.74$ s through the six different azimuthally limited seismic amplitude volumes. Figure 3 shows time slices through the six corresponding coherence volumes. Because the S/N of each azimuthal sector seismic amplitude is low, the S/N of the resulting coherence images is also low. The differences between the six azimuthally limited coherence images include the shape and size of karst features (indicated by green arrows), the continuity of subtle faults (indicated by yellow arrows), and the level of incoherent noise. As recognized by Perez and Marfurt (2008), faults are best delineated by the azimuths perpendicular to them (e.g., Figure 3a at 0° versus Figure 3c at 60°).

Stacking the six seismic amplitude volumes and then computing coherence (the conventional analysis workflow) gives the result shown in Figure 4a. This image shows an increased S/N but a slightly lower lateral resolution than the azimuthally limited coherence time slices shown in Figure 3. Figure 4b shows the result of stacking the six images shown in Figure 3. The resolution on Figure 4b is lower than that of Figure 4a; however, edges of the karst features appear more pronounced than on the traditional coherence computation. Figure 4c shows the multiazimuth coherence result computed using the covariance matrix described by equation 1. Note that multiazimuth coherence displays the higher spatial resolution than either traditional coherence or stacked azimuthal coherence, especially in areas with high anisotropy (indicated in Figure 4d). Karst features (indicated by green arrows) exhibit highly incoherent anomalies, whereas subtle faults (indicated by yellow arrows) appear as strong as the major faults. Multiazimuth coherence not only preserves most of the discontinuities seen in each of the azimuthally limited coherence volumes in Figure 3 but also suppresses incoherent noise. Figure 4e shows the RGB corendered azimuthally limited coherence 165°–15° (red), 45°–75° (green), and 105°–135° (blue). If the three input azimuthal coherence volumes were perfectly aligned, the coherent part of the corendered RGB image would be white and aligned faults would be black. In Figure 4e, most areas are well-aligned and are indicated by the white color; however, faults and karst collapse features are less well-aligned, and they are mapped by colors other than black. Magenta arrows indicate low coherence at 45°–75°, and the green arrow indicates low coherence at 105°–135°, whereas the black arrow indicates low coherence for all three input volumes. Note that areas with high anisotropy in Figure 4d give rise to colorful or misaligned anomalies in Figure 4e.

Survey B is also from the Fort Worth Basin, Texas. The data were prestack time migrated into eight azimuthal sectors at 22.5° intervals. Figure 5 shows time slices at $t = 1.36$ s through four of the coherence volumes 0°–22.5°, 45°–67.5°, 90°–112.5°, and 135°–157.5°. These data were migrated using an isotropic velocity model, such that anisotropy gives rise to lateral shifts (indicated by yellow arrows) in the coherence anomalies. Zhang et al. (2014, 2015) and Verma et al. (2016) apply a prestack structure-oriented filter to suppress coherent noise, processing, and migration artifacts. Perez and Marfurt (2008) apply a spatial crosscorrelation technique to the coherence slices to measure lateral shifts of discontinuities and then correct them using a data warping algorithm. Figure 6a illustrates a time slice through coherence computed from the stacked seismic amplitude volume. Note the S/N in Figure 6a is higher than that in Figure 5 because random noise is suppressed after stacking azimuthally limited seismic amplitude volumes. However, despite being noisy, the images in Figure 5 exhibit a higher lateral resolution than Figure 6a. Lateral shifts (indicated by yellow arrows) of discontinuities observed from different azimuthally limited coherence volumes have been smeared by stacking. In general, applying isotropic velocity to either area with anisotropic effects due to microcracks opening perpendicular to the minimum horizontal stress direction in this survey gives rise to azimuthal variations of discontinuities. Guo et al. (2016) compare

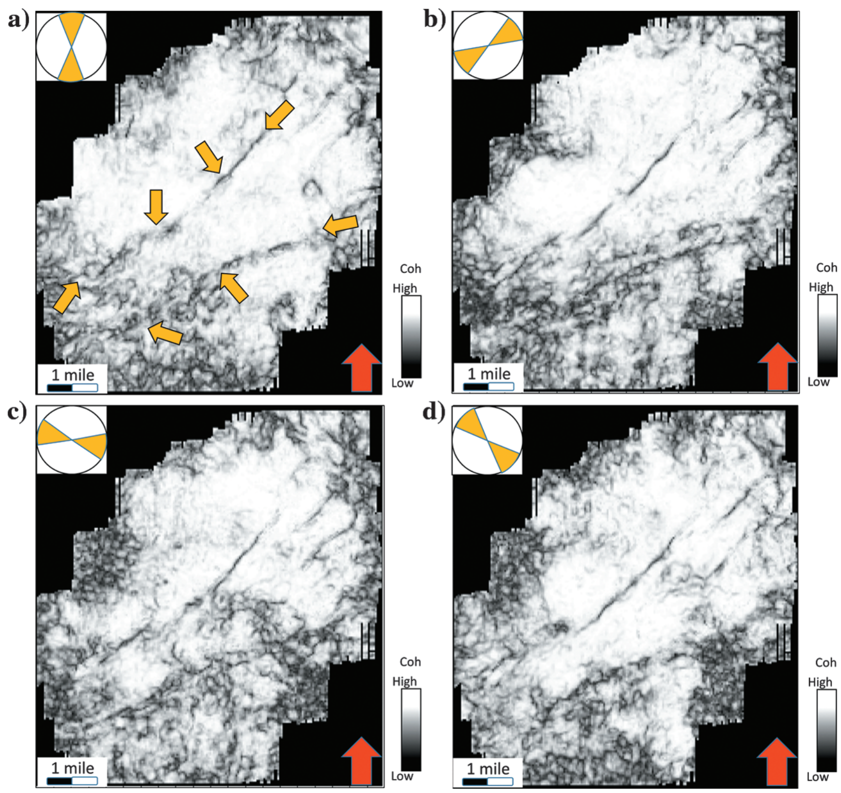

Figure 5. Time slices at $t = 1.36$ s through the coherence volume computed from the azimuthal sector (a) 0°–22.5°, (b) 45°–67.5°, (c) 90°–112.5°, and (d) 135°–157.5° in the second data set. Note that there are significant differences between each azimuthal coherence. The lateral shifts of the discontinuities are indicated by the yellow arrows.

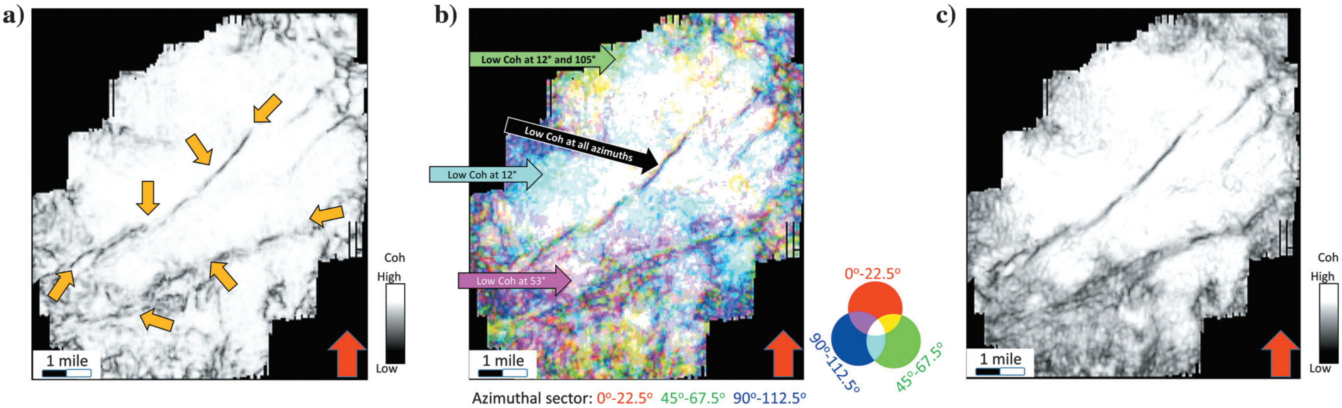

Figure 6. Time slices at $t = 1.36$ s through (a) the poststack coherence volume, (b) the RGB image computed by azimuthal sectors 0°–22.5°, 45°–67.5°, and 90°–112.5°, and (c) the new multiazimuth coherence. Note that there are significant improvements in the delineation of lateral shifted faults (indicated by yellow arrows) in the multiazimuth coherence. Lateral resolution especially in less coherent areas has been improved.

these data (before hydraulic fracturing) with adjacent data (after hydraulic fracturing), and find that these data exhibit strong anisotropic effects along faults by correlating the most-positive curvature and amplitude variation with azimuth anisotropy. Figure 6b shows the corendered RGB plot of azimuthally limited coherence volumes 0°–22.5° (red), 45°–67.5° (green), and 90°–112.5° (blue). Areas that appear to be magenta indicate that the azimuthal coherence volume 0°–22.5° is less coherent than the other two volumes. Areas that appear to be blue indicate that the coherence from the 90°–112.5° volume is less coherent. Figure 6c shows the multiazimuth coherence attribute. Comparison with Figure 6a–6c describes a significant improvement in the delineation of areas that was laterally shifted (indicated by yellow arrows). The two major faults exhibit strongly incoherent anomalies. Figure 6b and 6c indicates similar discontinuous anomalies, but Figure 6c exhibits a higher S/N. Lateral resolution, especially in less coherent areas, has increased.

CONCLUSION

We have introduced a new way to compute coherence of azimuthal sectors that preserves subtle discontinuities seen on the individual azimuthal volumes. The new multiazimuth coherence can avoid smearing lateral variations and suppress incoherent noise. The algorithm consists of computing a covariance matrix for each azimuthal sector and summing the results. Eigendecomposition of the summed covariance matrix of all azimuthally limited volumes is a nonlinear process, such that the first eigenvector of the summed covariance matrix is not a linear combination of the first eigenvectors computed for the azimuthally limited covariance matrix. The summed covariance matrix provides a superior image to those provided by stacking the data and computing coherence, or by stacking the coherence computed from each azimuthally limited seismic volume. Compared with traditional coherence or the stacked azimuthal coherence, the multiazimuth coherence displays higher lateral resolution and better delineates karst collapse features and subtle faults. Although RGB blending can only corender three attribute volumes at a time, it provides a powerful tool that measures imaging problems associated with anisotropy. Survey A from the southwest part of the Fort Worth Basin exhibits only moderate azimuthal anisotropy. Fault images at different azimuths align in the RGB images and appear black, whereas the elliptical collapse features express a color that favors the azimuth perpendicular to the orientation of the edge. Survey B from the northeast part of the Fort Worth Basin straddles the Mineral Wells Fault and exhibits considerable anisotropy. Therefore, the fault images are misaligned and appear as a suite of red, green, and blue anomalies. Summing the corresponding misaligned covariance matrices results in a blurred coherence image. Although the improvement over coherence computed from the stacked data is minimal, we hypothesize that addressing these misalignment issues may provide a future tool for anisotropic velocity analysis and quality control measures.

ACKNOWLEDGMENTS

The authors would like to thank Marathon Oil and Devon Energy for providing licenses for their data. We also appreciate the financial support from the University of Oklahoma Attribute-Assisted Seismic Processing and Interpretation (AASPI Consortium).

APPENDIX A

ENERGY-RATIO COHERENCE

The covariance matrix is constructed from a suite of sample vectors that are parallel to the structural dip. The covariance matrix for this analysis window is

$$\mathbf{C}_{mn} = \sum_{k=-K}^{+K} (\mathbf{d}_{km}\mathbf{d}_{kn} + \mathbf{d}^{\mathrm{H}}_{km}\mathbf{d}^{\mathrm{H}}_{kn}), \tag{A-1}$$

where the superscript H denotes the Hilbert transform along the traces and the subscripts m and n are indices of input traces $(1,2, \ldots, M)$. For example, element C_{23} in the covariance matrix $\mathbf{C}_{mn}$ is $\sum_{k=-K}^{+K} (\mathbf{d}_{k2}\mathbf{d}_{k3} + \mathbf{d}^{\mathrm{H}}_{k2}\mathbf{d}^{\mathrm{H}}_{k3})$. The Hilbert transform (90° phase rotated) version of the data does not modify the vertical resolution but improves areas of low S/N about the zero crossing (Marfurt, 2006). The first eigenvector $\mathbf{v}^{(1)}$ of the covariance matrix $\mathbf{C}$ best represents the lateral variation of each sample vector of the constituent.

Crosscorrelating this eigenvector with the kth sample vector that includes the analysis point gives a crosscorrelation coefficient β_k:

$$\beta_k = \sum_{m=1}^{M} \mathbf{d}_{km} \mathbf{v}_m^{(1)}. \tag{A-2}$$

The principal component (Karhunen-Loève) filtered data within the analysis window are then

$$\mathbf{d}_{km}^{\mathrm{KL}} = \beta_k \mathbf{v}_m^{(1)}. \tag{A-3}$$

Note that in Figure 1, the wavelet amplitude of the three leftmost traces is about two times larger than that of the two rightmost traces. After filtering, this proportion is preserved.

Energy-ratio coherence computes the ratio of the coherent energy and the total energy in an analysis window:

$$C_{\mathrm{ER}} = \frac{E_{\mathrm{coh}}}{E_{\mathrm{tot}} + \varepsilon^2}, \tag{A-4}$$

where the coherent energy E_{coh} (the energy of the KL-filtered data) is

$$E_{\mathrm{coh}} = \sum_{k=-K}^{+K} \sum_{m=1}^{M} [(\mathbf{d}_{km}^{\mathrm{KL}})^2 + (\mathbf{d}_{km}^{H\mathrm{KL}})^2], \tag{A-5}$$

whereas the total energy E_{tot} of unfiltered data in the analysis window is

$$E_{\mathrm{tot}} = \sum_{k=-K}^{+K} \sum_{m=1}^{M} [(\mathbf{d}_{km})^2 + (\mathbf{d}_{km}^{H})^2], \tag{A-6}$$

and where a small positive value ε prevents division by zero.

REFERENCES

Al-Dossary, S., Y. Simon, and K. J. Marfurt, 2004, Interazimuth coherence attributes for fracture detection: 74th Annual International Meeting, SEG, Expanded Abstracts, 183–186.

Bahorich, M. S., and S. L. Farmer, 1995, 3-D seismic discontinuity for faults and stratigraphic features: The Leading Edge, **14**, 1053–1058, doi: 10.1190/1.1437077.

Bakker, P., 2002, Image structure analysis for seismic interpretation: Ph.D. thesis, Delft University of Technology.

Barnes, A. E., 2000, Weighted average seismic attributes: Geophysics, **65**, 275–285, doi: 10.1190/1.1444718.

Bednar, J. B., 1998, Least-squares dip and coherency attributes: The Leading Edge, **17**, 775–778, doi: 10.1190/1.1438051.

Chopra, S., and K. J. Marfurt, 2007, Seismic attributes for prospect identification and reservoir characterization: SEG.

Gersztenkorn, A., and K. J. Marfurt, 1999, Eigenstructure based coherence computations as an aid to 3D structural and stratigraphic mapping: Geophysics, **64**, 1468–1479, doi: 10.1190/1.1444651.

Guo, S., S. Verma, Q. Wang, B. Zhang, and K. J. Marfurt, 2016, Vector correlation of amplitude variation with azimuth and curvature in a post-hydraulic-fracture Barnett Shale survey: Interpretation, **4**, no. 1, SB23–SB35, doi: 10.1190/INT-2015-0103.1.

Hale, D., 2013, Methods to compute fault images, extract fault surfaces, and estimate fault throws from 3D seismic images: Geophysics, **78**, no. 2, O33–O43, doi: 10.1190/geo2012-0331.1.

Kington, J., 2015, Semblance, coherence, and other discontinuity attributes: The Leading Edge, **34**, 1510–1512, doi: 10.1190/tle34121510.1.

Li, F., and W. Lu, 2014, Coherence attribute at different spectral scales: Interpretation, **2**, no. 1, SA99–SA106, doi: 10.1190/INT-2013-0089.1.

Li, F., J. Qi, and K. J. Marfurt, 2015, Attribute mapping of variable thickness incised valley-fill systems: The Leading Edge, **34**, 48–52, doi: 10.1190/tle34010048.1.

Luo, Y., S. al-Dossary, M. Marhoon, and M. Alfaraj, 2003, Generalized Hilbert transform and its application in geophysics: The Leading Edge, **22**, 198–202, doi: 10.1190/1.1564522.

Luo, Y., W. G. Higgs, and W. S. Kowalik, 1996, Edge detection and stratigraphic analysis using 3D seismic data: 66th Annual International Meeting, SEG, Expanded Abstracts, 324–327.

Marfurt, K. J., 2006, Robust estimates of 3D reflector dip and azimuth: Geophysics, **71**, no. 4, P29–P40, doi: 10.1190/1.2213049.

Marfurt, K. J., 2017, Interpretational value of multispectral coherence: 79th Annual International Conference and Exhibition, EAGE, Extended Abstracts, doi: 10.3997/2214-4609.201700528.

Marfurt, K. J., R. L. Kirlin, S. H. Farmer, and M. S. Bahorich, 1998, 3D seismic attributes using a running window semblance-based algorithm: Geophysics, **63**, 1150–1165, doi: 10.1190/1.1444415.

Perez, G., and K. J. Marfurt, 2008, Warping prestack imaged data to improve stack quality and resolution: Geophysics, **73**, no. 2, P1–P7, doi: 10.1190/1.2829986.

Perez, M., R. Gibson, and M. N. Toksöz, 1999, Detection of fracture orientation using azimuthal variation of P-wave AVO response: Geophysics, **64**, 1253–1265, doi: 10.1190/1.1444632.

Qi, J., B. Zhang, H. Zhou, and K. J. Marfurt, 2014, Attribute expression of fault-controlled karst — Fort Worth Basin, TX: Interpretation, **2**, no. 3, SF91–SF110, doi: 10.1190/INT-2013-0188.1.

Qi, J., T. Lin, T. Zhao, F. Li, and K. J. Marfurt, 2016, Semisupervised multiattribute seismic facies analysis: Interpretation, **4**, no. 1, SB91–SB106, doi: 10.1190/INT-2015-0098.1.

Roende, H., C. Meeder, J. Allen, S. Peterson, and D. Eubanks, 2008, Estimating subsurface stress direction and intensity from subsurface full-azimuth land data: 78th Annual International Meeting, SEG, Expanded Abstracts, 217–220.

Schuelke, J. S., 2011, Overview of seismic attribute analysis in shale play: Attributes: New views on seismic imaging: Their use in exploration and production: Presented at the 31st Annual GCSSEPM Foundation Bob F. Perkins Research Conference.

Sui, J.-K., X. Zheng, and Y. Li, 2015, A seismic coherency method using spectral attributes: Applied Geophysics, **12**, 353–361, doi: 10.1007/s11770-015-0501-5.

Sullivan, E. C., K. J. Marfurt, A. Lacazette, and M. Ammerman, 2006, Application of new seismic attributes to collapse chimneys in the Fort Worth basin: Geophysics, **71**, no. 4, B111–B119, doi: 10.1190/1.2216189.

Verma, S., S. Guo, and K. J. Marfurt, 2016, Data conditioning of legacy seismic using migration-driven 5D interpolation: Interpretation, **4**, no. 2, SG31–SG40, doi: 10.1190/INT-2015-0157.1.

Wu, X., 2017, Directional structure-tensor-based coherence to detect seismic faults and channels: Geophysics, **82**, no. 2, A13–A17, doi: 10.1190/geo2016-0473.1.

Wu, X., and D. Hale, 2016, 3D seismic image processing for faults: Geophysics, **81**, no. 2, IM1–IM11, doi: 10.1190/geo2015-0380.1.

Wu, X., S. Luo, and D. Hale, 2016, Moving faults while unfaulting 3D seismic images: Geophysics, **81**, no. 2, IM25–IM33, doi: 10.1190/geo2015-0381.1.

Zhang, B., D. Chang, T. Lin, and K. J. Marfurt, 2015, Improving the quality of prestack inversion by prestack data conditioning: Interpretation, **3**, no. 1, T5–T12, doi: 10.1190/INT-2014-0124.1.

Zhang, B., T. Zhao, J. Qi, and K. J. Marfurt, 2014, Horizon-based semiautomated nonhyperbolic velocity analysis: Geophysics, **79**, no. 6, U15–U23, doi: 10.1190/geo2014-0112.1.